Freestanding Sodium-Ion Batteries Electrode Using Graphene Foam Coaxially Integrated with TiO$_2$ Nanosheets

Gaoxiang Wu,[a] Jiewei Chen,[a] Yanjiao Guo,[a] Xiaodan Li,[b] Bi Luo,[a] Lihua Chu,[a] Yu Han,[c] Bing Jiang,[a] Li Xu,[c] and Meicheng Li[a,z]

[a]*State Key Laboratory of Alternate Electrical Power System with Renewable Energy Sources, School of Renewable Energy, North China Electric Power University, Beijing 102206, People's Republic of China*
[b]*Key Laboratory of Functional Materials and Applications of Fujian Province, School of Materials Science and Engineering, Xiamen University of Technology, Xiamen 361024, People's Republic of China*
[c]*Material Laboratory of State Grid Corporation of China, State Key Laboratory of Advanced Transmission Technology, Global Energy Interconnection Research Institute, Beijing 102209, People's Republic of China*

Sodium-ion batteries (SIBs) have attracted great interests for use as the large-scale rechargeable batteries, in which electrode materials are the most crucial components. Here, an ingenious programming of freestanding electrode material is reported for SIBs, which consists of titanium dioxide nanosheets aligned vertically on graphene foams (GF) framework inside and outside forming coaxial frame structure (GF-CF). This frame architecture not only ensures sufficient contact area between active materials and electrolyte but also is beneficial to fast electron transportation. Moreover, the titanium dioxide nanosheets in situ grew on GF, which can inhibit the aggregation of nanosheets and improve the electrochemical kinetics. As freestanding anode material for SIBs, GF-CF exhibits high capacity retention (88.0%) at 50 mA g^{-1} after 100 cycles and improved rate performance. We also find that ∼45.1% of the total sodium-ion storage comes from capacitive contribution, which could be further improved by diminishing the size of TiO$_2$ nanosheets. The approach of building the desirable coaxial frame structure can be extendedly applied to the architectural construction of electrode materials for other energy devices.
© 2017 The Electrochemical Society. [DOI: 10.1149/2.0721713jes] All rights reserved.

Lithium-ion batteries (LIBs) have been widely applied to electric vehicles (EVs) and consumer electronics such as mobile phones, laptops to cope with the issue of the exhaustion of non-renewable resources and the environmental problems, because of their excellent energy density, long lifetime and good rate capability.[1–6] However, it is a great pressure to meet the demand for large-scale energy storage and smart grid applications from limited lithium resources.[7] As an alternative, sodium exhibits many similar physicochemical properties with lithium and other particular advantages. For instance, sodium is rich in natural resource. Furthermore, the standard electrode potential of Na$^+$/Na is −2.7 V which is 0.3 V higher than that of Li$^+$/Li (−3.0 V), which can use aluminum as anode current collectors instead of copper to lower costs. Because aluminum undergoes alloy reaction with lithium below 0.1 V vs. Li$^+$/Li.[8] Consequently, sodium-ion batteries (SIBs) have logically been expected as the best candidate for the next generation rechargeable batteries.[7] However, the larger size of sodium ion (1.02 Å) compared with lithium ion (0.76 Å) makes it hard to find applicable electrode materials for SIBs.[9]

With regard to anode materials, graphite has been proved to be the most successful anode materials for LIBs, but when used for SIBs, the capacity is not satisfactory.[10,11] P, S and Sb et al. as well as their alloy based composites have satisfied theoretical capacity,[12–14] but the volume change during repeated charge/discharge is so huge that their applications for SIBs are difficult. Among numerous of metal oxides, TiO$_2$ is one of the promising candidate anode material for SIBs because of low price and stable structure during repeated charge/discharge process.[15–17] Especially, the safety performance has been improved because sodium dendrite will not grow. Nevertheless, rate performance of TiO$_2$ leaves much to be desired because of its low electronic conductivity.[18–20]

Researchers have made many efforts to improve the ionic and electrical conductivity of the TiO$_2$-based anodes, including designing nano-sized TiO$_2$ and introducing carbon additives.[21,22] Generally, TiO$_2$ will be integrated with graphene oxide[23,24] because there are many functional group on oxide graphene so that TiO$_2$ could grow on it easily, but the electric conductivity of graphene oxide and reduced graphene oxide is poorer than that of graphene which synthesized

by chemical vapor deposition.[25–28] In regard to these problems, we design TiO$_2$-based materials that generated on graphene. Furthermore, current collectors, conductive agents and binders that used in traditional preparation process actually increase the total weight and cost.[29]

Here, we report a coaxial frame architecture of TiO$_2$ connected to graphene foams (GF-CF) to prepare freestanding anode material for SIBs firstly with high capacity retention (88.5%) and desirable rate performance. In GF-CF composite electrode, dense TiO$_2$ nanosheets were vertically in situ aligned on graphene foams framework inside and outside forming coaxial frame structure. This coaxial frame structure of TiO$_2$ and graphene in an appropriate pattern can provide well electronic connection between them. At the same time producing more active sites for sodium storage due to the large interface between graphene and TiO$_2$. Meantime, the freestanding GF-CF electrode can be directly assembled without current collector, conductive agent and binder, so reducing the cost and overcoming the adverse side reactions caused by these inactive components. In order to investigate the electrochemical kinetics of GF-CF toward Na$^+$, particular voltammetric analysis has been used to quantify the dependence of the pseudocapacitance.

Experimental

Materials synthesis—Chemicals.—Nickel foams were purchased from Alantum Advanced Technology Materials (Shenyang). Anatase TiO$_2$, Normal propyl alcohol, tetrabutyl titanate (TBOT), hydrofluoric acid (HF) and sodium were obtained from Sigma-Aldrich. PVDF was purchased from Arkema. Copper foil was purchased from Guangdong Fine Yuan Science Technology CO.LTD. NaClO$_4$, ethylene carbonate (EC), dimethyl carbonate (DMC) and N-methyl-2-pyrrolidone (NMP) were purchased from Alfa Aesar. All of the chemical reagents were used as received without further purification.

Preparation of GF.—Nickel foams used as 3D scaffold templates were heated to 1000°C for 10 min in a horizontal tube furnace (Lindberg Blue M, TF55030C) under the gas atmosphere of H$_2$ (200 sccm.) and Ar (500 sccm.) to clean the surfaces and reduce the oxide layer. Then CH$_4$ (5 sccm.) was introduced into the reaction tube at ambient pressure for 5 min. Then, turn off CH$_4$ and let samples cool to room temperature under H$_2$ (200 sccm.) and Ar (500 sccm.). Afterwards, drop polymethyl methacrylate (PMMA) solution (4.5% in acetidin)

[z]E-mail: mcli@ncepu.edu.cn

onto Ni foams that coated with graphene and heat the samples to 110°C for 30 min. The Ni foam@graphene@PMMA was obtained after solidification. Then, Ni foam was completely dissolved by putting Ni foam@graphene@PMMA into a 3 M HCl solutions for 3 hours at 80°C, as a result graphene foam@PMMA was obtained. Finally, GF was obtained by hotting graphene foam@PMMA in acetone at 55°C to remove PMMA.

Preparation of GF-CF.—A facile hydrothermal synthesis method be used to prepare GF-CF. Firstly, 2 mL of TBOT and 0.8 mL of HF were orderly added into 25 mL of Normal propyl alcohol with constant magnetic stirring for 20 min. Secondly, transfer this reaction solution into teflon-lined stainless steel autoclave and immerse the graphene foam at the same time. After maintaining 24 h at 180°C in an electric oven, the autoclave was left to cool down to room temperature. Finally, the graphene foam coated with a TiO_2 was washed with deionized water and ethanol for several times and dried in a freeze dryer at −50°C for 48 h to obtain GF-CF.

Characterization.—The morphology, size and distribution of the specimens were characterized by HITACHI SU8010 microscope field emission scanning electron microscope (FESEM) and Tecnai G2 F20 field emission transmission electron microscopy (TEM) with an accelerating voltage of 200 kV. Thermogravimetric analysis (TGA, Mettler Toledo TGA/DSC 3+) was carried out in air atmosphere from 30 to 1100°C at a temperature rate of 10°C min^{-1}. The chemical compositions and structures of GF and GF-CF were analyzed by X-ray diffraction (XRD) (Bruker D8 Advance X-ray diffractometer, Cu-Kα radiation λ = 0.154 nm). X-ray photoelectron spectroscopy (XPS) measurements were performed at the ESCALAB 250Xi X-ray photoelectron spectroscope equipped with Al Kα radiation. Raman spectra was investigated with the equipment Horiba Jobin Yvon(HJY) LabRAM.

Electrochemical measurements.—Standard CR2032-type coin cells were assembled in an Ar-filled glove box that has both oxygen and moisture concentration below 0.01 ppm by using GF-CF, GF or anatase TiO_2 anode, sodium metal foil with the thickness of ∼0.6 mm as the reference and counter electrode, glass nanofiber (Whatman) as separator. Here we used two kinds of working electrodes. The one was anatase TiO_2 electrode fabricated by coating a slurry containing 10 wt% of PVDF, 20 wt% of acetylene black (Super-P), and 70 wt% of active materials (anatase TiO_2) dissolved in NMP onto a copper foil and drying at 70°C for 5 h in vacuum (10^{-3} Torr). Afterwards the specimens were dried at 110°C in vacuum for 10 h after pressing before assembling. The average mass loading of active materials was about 1 mg cm^{-2} in this electrode. Another one was GF-CF and GF electrodes without conductive agents, binders and copper. The electrolyte was 1 M $NaClO_4$ dissolved in a mixture of EC and DMC (v/v = 1:1). The average mass loading of GF-CF and GF electrodes was about 1.9 and 0.5 mg cm^{-2}, respectively.Before starting electrochemical measurements, cells were aged for 15 h. Electrochemical impedance spectra (EIS) were measured using an electrochemical workstation (Zahner Zennium) by applying an AC voltage of 10 mV amplitude over the frequency range from 0.1 Hz to 100 kHz. Galvanostatic discharge-charge (GDC) experiments were tested in the voltage window of 0.10–2.00 V vs Na$^+$/Na at different specific currents with a multichannel battery system (Land, China). Cyclic voltammetry (CV) measurements were performed on an electrochemical workstation (CHI660e, Shanghai Chenhua).

Results and Discussion

GF-CF was prepared by a two-step process. The first step is chemical vapor deposition to grow graphene foam. In this step the electric conduction framework will be built. The second step is hydrothermal reaction to form TiO_2 nanosheets that coaxially generated on graphene foam. The formation mechanism of GF-CF is shown in Fig. 1. Resembling the previous reports,[30,31] nickel foam was served as a template and carbon was introduced by decomposing CH_4 at 1000°C under atmospheric pressure. Afterwards, remove nickel substrate using 3 M HCl to get the graphene foam. In the end, TiO_2 on the outside and inside of graphene foam was synthesized via a hydrothermal process forming coaxial frame structure.

According to scanning electron microscopy (SEM) for GF-CF, three-dimensional microtube-connected framework built by graphene foams could be distinctly observed with a width of ∼50 μm in Figs. 2a and 2b. From SEM images of Ni foams and Ni foams@graphene (Fig. S1), we found that there is no significant difference in morphology between Ni foams, Ni foams@graphene, GF and GF-CF. The higher magnification image of SEM (Fig. 2c and the inset of Fig. 2c) reveals that numerous nanosheets have grown on inside and outside of the graphene, which just like a sandwich microstructure. A nanoporous feature created by the gap of nanosheets could be observed in Figs. 2c and 2d, and these TiO_2 nanosheets show the length and thickness with about 50 and 10 nm, respectively. In the high-resolution TEM image (the inset of Fig. 2d), there are clear lattices with spacing of 0.35 nm, indicating the existence of anatase TiO_2. The Raman spectra (Fig. 2e) of GF have two representative bands located at ∼1580, and 2700 cm^{-1}, corresponding to the G, and 2D bands, respectively. The G band, which is a doubly degenerate (TO and LO) phonon mode (E_{2g} symmetry) at the Brillouin zone center, originates from in-plane vibration of sp^2 carbon atoms.[32] The 2D band, which is the second order of zone-boundary phonons historically named G', originates from a two phonon double resonance Raman process.[32,33] From the intensity ratio of the G and 2D bands, we can know that GF is made up of a few layers of graphene.[34] There is no D band in the vicinity of 1350 cm^{-1} at the detected level, which suggests the high quality and defect free of GF.[35] Moreover, GF-CF shows additional bands at ∼142, 396, 517, and 639 cm^{-1}, representing the E_g, B_{1g}, A_{1g}, and E_{1g} bands of the typical anatase TiO_2.[36] In addition, a broad D band, the breathing mode of κ-point phonons of A_{1g} symmetry, appears at ∼1350 cm^{-1} for GF-CF. Which is associated with vibrations of carbon atoms with dangling bonds.[37] The appearance of weak D band indicated a few carbonaceous defects generation after hydrothermal treatment. Consequently, these results proved that the TiO_2 nanosheets could anchor on the surface of GF, while maintaining the crystallinity of GF. The loading percentage of TiO_2 on GF-CF and thermal stability of GF-CF were measured through a thermogravimetric analysis (TGA) in air (Fig. 2f). ∼6% weight loss before 300°C is associated with the evaporation of water, whereas ∼20% weight loss between 300–900°C is assigned to the combustion of graphene. So it was clearly that the loading ratio of TiO_2 on GF-CF was 74%. From the above, these results suggest the successfully establishment of coaxial frame structure.

To investigate the surface composition and chemical state of GF and GF-CF, XRD and XPS analyses were put to use. Fig. 3a shows the XRD patterns of GF and GF-CF. The GF has two distinct diffractions peaks at ∼26.5° and ∼54.7° attributed to the (002) and (004) reflections of graphitic carbon, respectively (JCPDS 75-1621). In addition to the characteristic peaks from graphene, the GF-CF presents crystal peaks at ∼25.3°, ∼37.9°, ∼48.0°, ∼54.5° and ∼62.2°, corresponding to (101), (004), (200), (105) (and (211)) and (211) crystal faces, respectively, which can be indexed to tetragonal anatase TiO_2 (JCPDS 21-1272). Furthermore, Fig. 3b shows the survey scans of GF-CF and GF. GF consists of two peaks, a shallow O 1s peak and a sharp C 1s peak located at ∼530.5 eV and ∼284.4 eV, respectively. After hydrothermal process, an additional Ti 2p and an enhanced O 1s peak were observed, which demonstrate that TiO_2 nanosheets were well decorated on GF network. As shown in Figs. 3c–3f, high-resolution C 1s, Ti 2p, and O 1s XPS spectra of GF and GF-CF were taken to clarify the detailed bonding characteristics. C 1s peak of GF at ∼284.4 eV is sharp, as shown in Fig. 3f, the carbon content comprises of 81.4% at 284.4 eV corresponding to the C-C (and C=C) bonds and 19.6% at 285.2 eV corresponding to C–O (and C=O) bonds. As a result the C=C and C-C bonds on GF are strong. Correspondingly,
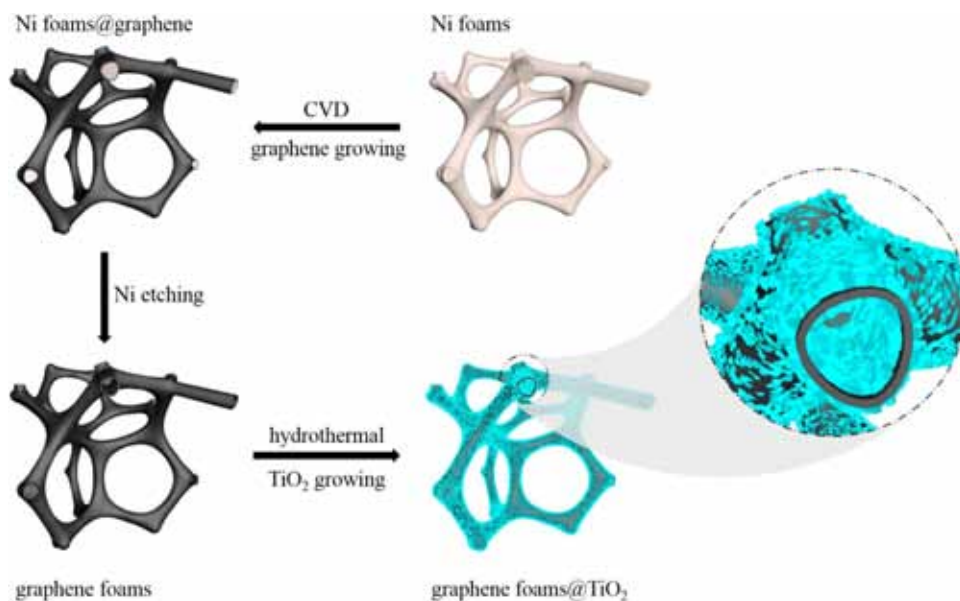
Figure 1. Schematic illustration of GF-CF fabrication via CVD and hydrothermal reaction.
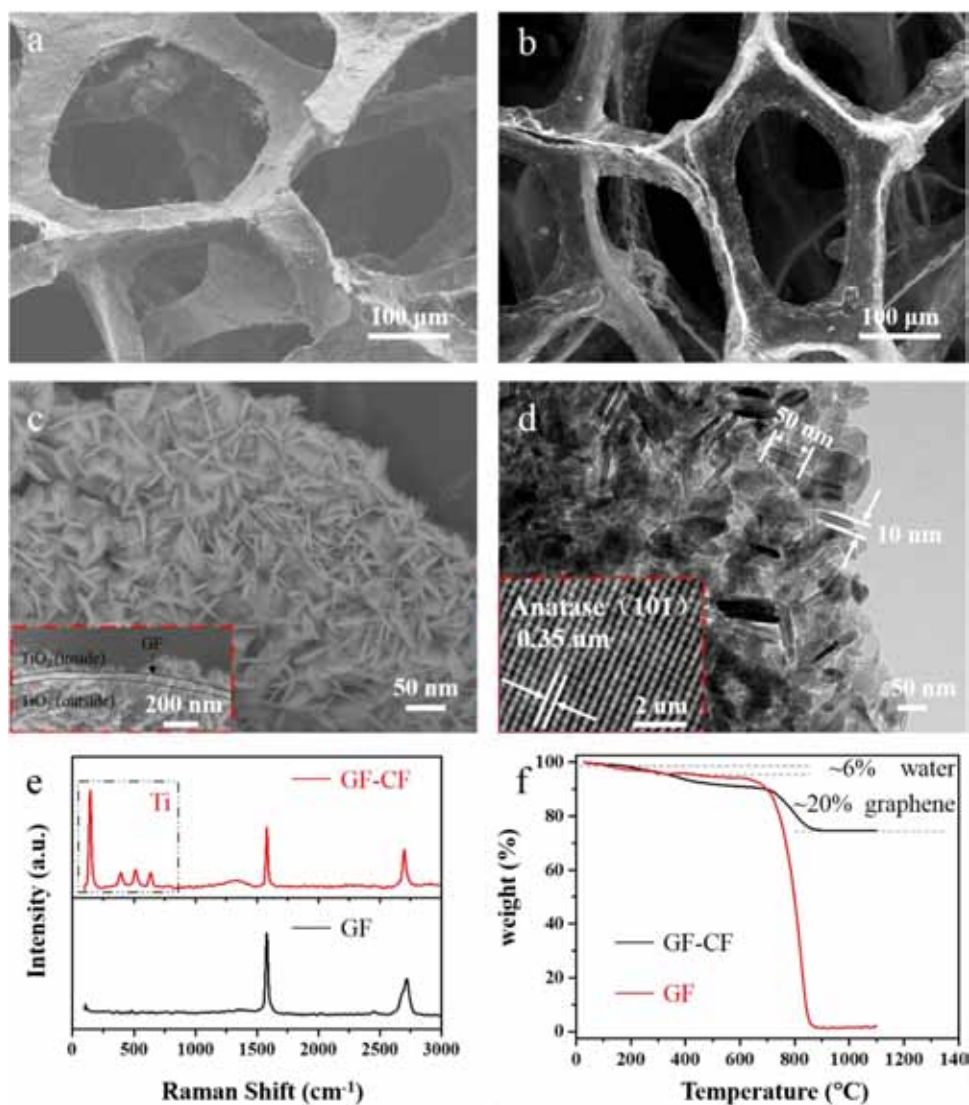

Figure 2. Morphology and structure of GF-CF and GF. SEM images for GF-CF (a) and GF (b); (c) SEM images for GF-CF (inset of c: the edge of GF-CF); (d) TEM image for GF-CF (inset: High-resolution TEM image for GF-CF); (e) Raman spectra of GF-CF and GF; (f) thermogravimetric curves of GF-CF and GF..
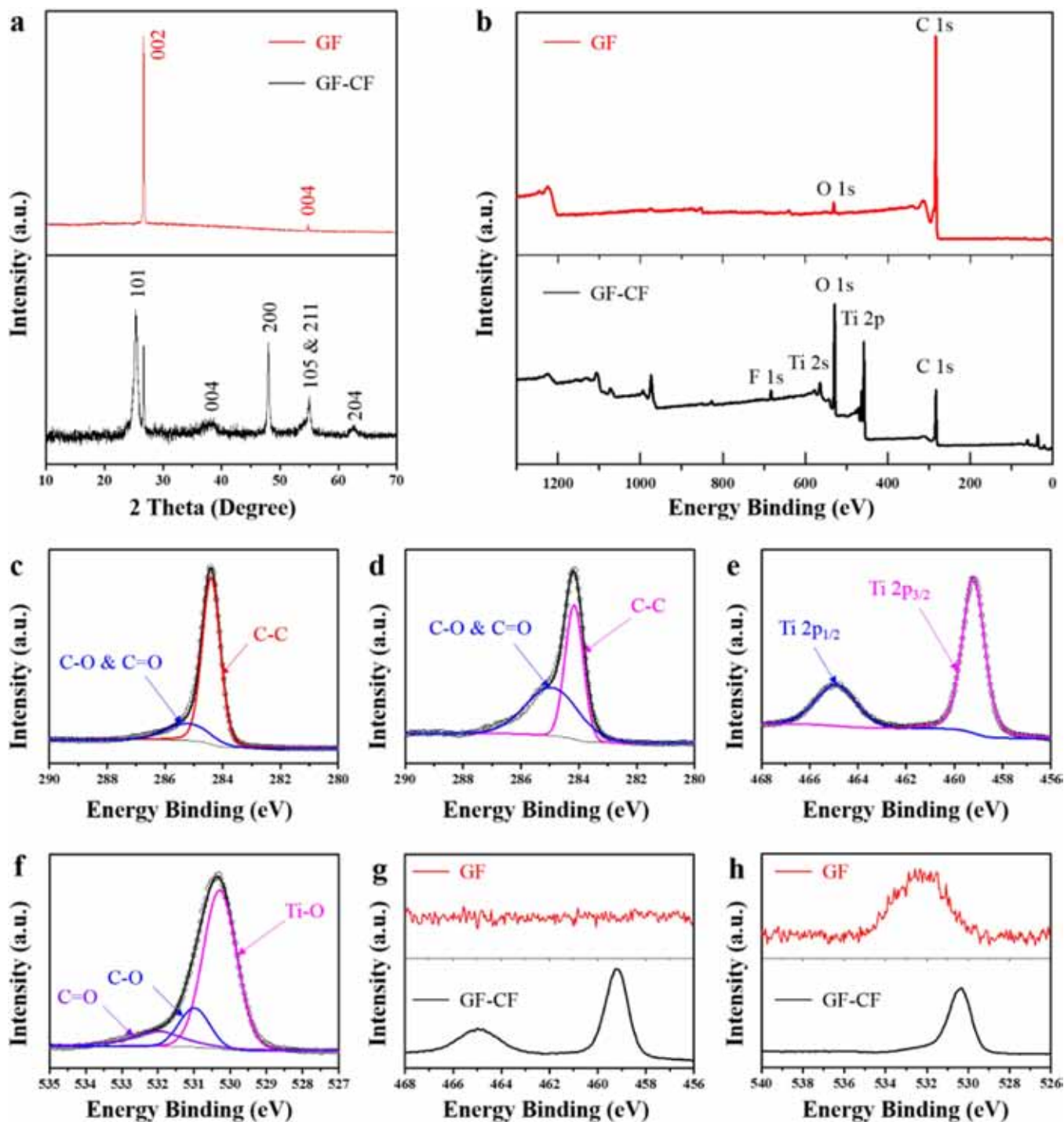
Figure 3. Surface composition and chemical state of GF and GF-CF. (a) XRD patterns and (b) XPS spectra of GF and GF-CF; high-resolution XPS spectra of GF: (c) C 1s; high-resolution XPS spectra of GF-CF: (d) C 1s, (e) Ti 2p, and (f) O 1s; comparison of high-resolution XPS spectra of GF and GF-CF: (g) Ti 2p, and (h) O 1s.

there are also two peaks at 284.4 and 285.2 eV in the XPS spectra of GF-CF (Fig. 3d). But the ratio of C–O (and C=O) bonds increased remarkably. This change in the C 1s spectra is attributed to the TiO_2 nanosheets anchored onto GF forming the C-O-Ti bond during the hydrothermal treatment. Peaks located at about 458.9 and 464.7 eV could be observed for GF-CF samples which representing Ti $2p_{3/2}$ and $2p_{1/2}$ peaks of Ti^{4+} in TiO_2 (Fig. 3e), but Ti 2p peak cannot been found in the spectra of GF (Fig. 3g). Furthermore, in Fig. 3f, a sharp peak at 530.2 eV representing Ti-O bonds in TiO_2 and a weak peak at 532.0 eV corresponding to C=O bond on GF could be observed. Sig-

nificantly, the peak located at about 531.0 is attributed to C-O bonds, which further proved the existence of C-O-Ti bond. Because of the existence of carbonyl groups generated during Ni etching process, GF shows a weak peak at 532.0 eV, as shown in Fig. 3h. These results suggest that TiO_2 nanosheets bonded with GF chemically rather than adsorbed physically.

Na half-cells were assembled using GF-CF, anatase TiO_2 and GF to investigate the electrochemical performance. Electrochemical impedance spectra (EIS) (Fig. 4a) measurements were carried out to elucidate the Na^+ transfer behaviors of GF-CF, anatase TiO_2 and GF.
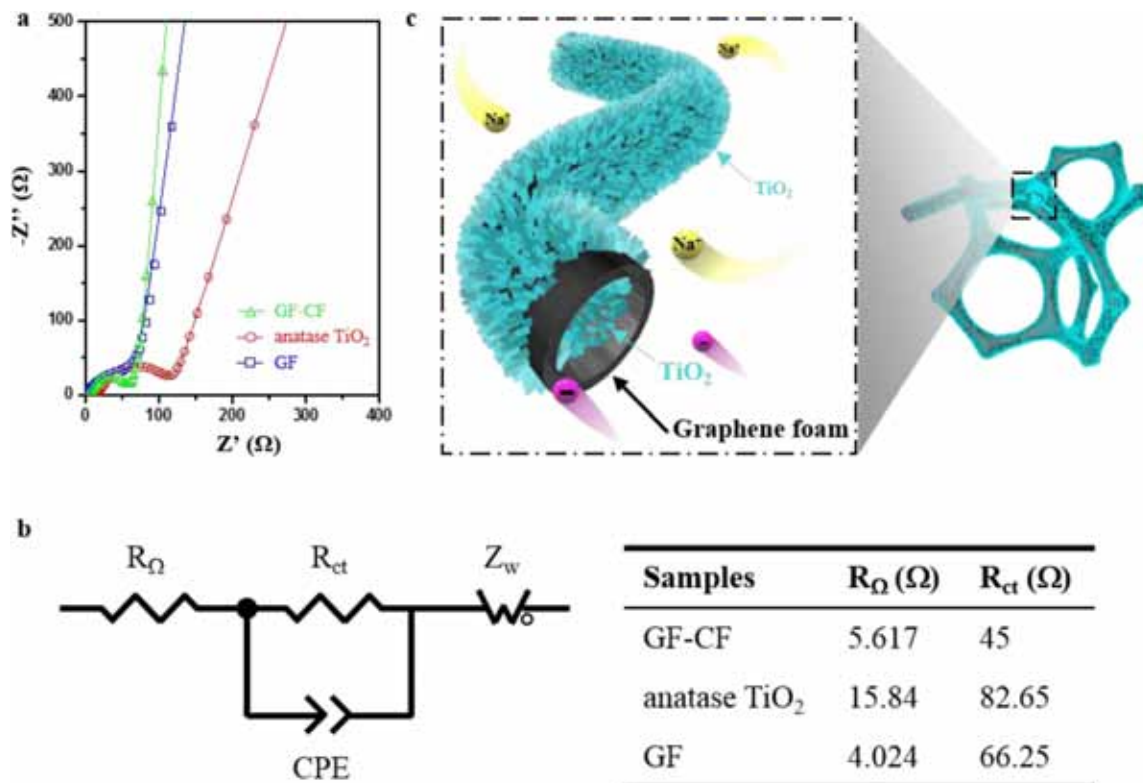
Figure 4. Resistance of GF-CF, anatase TiO$_2$ and GF electrodes. (a) EIS of GF-CF, anatase TiO$_2$ and GF; (b) the equivalent circuit model and fitting results of EIS; (c) schematic illustration displaying the transportation of sodium-ions and electrons in GF-CF.

The whole Nyquist plot contained a semicircle in the medium-high frequency area and a slope line in the low frequency zone. Based on the plot, the ohmic resistance (R$_\Omega$) of GF-CF is smaller than that of anatase TiO$_2$ mixed with binders and conducting agents and approximate to that of GF. Furthermore, GF-CF also has a much smaller diameter in the semicircle corresponding to the medium frequency range, which means the charge transfer resistance (R$_{ct}$) through the interface between electrode and electrolyte is lower. The corresponding equivalent circuit model and fitting results are displayed in Fig. 4b. These improved electrochemical performances are attributed to the coaxial frame structure of GF-CF. As illustrated in Fig. 4c, TiO$_2$ nanosheets inside and outside connected with graphene foam which offers stereoscopic conducting framework that facilitates electronic transport, thus resulting in lower charge transfer resistance and better electrical contacts. TiO$_2$ nanosheets which provides short diffusion path lengths vertically aligned on graphene foam in a form that simultaneously insured fast transportation of ions and electrons, reducing the kinetic restrictions. So the coaxial frame structure has accelerated the transportation of charge carriers.

Many researches have studied the electrochemical kinetics character of electrode materials by using cyclic voltammetry (CV) method toward Na$^+$.[38–40] Here, we used CV analysis to gain further electrochemical characteristics of GF-CF/Na cells. The initial five representative CV curves of GF-CF electrode at the scan rate of 0.1 mV s^{-1} were shown in Fig. 5a. In the first scan, the cathodic peak located at ∼0.5 V is due to a number of electrochemical reactions including the insertion of sodium-ion to the active materials and the SEI formation generated by electrolyte decomposition.[41] There is a cathodic peak located at ∼0.75 V and an anodic peak located at ∼0.84 V in the later scan with a small voltage excursion of 0.09 V. 4th and 5th curves have a good repeatability, indicating the excellent reversibility of GF-CF electrode. A series of alike shapes of peaks of CV curves during both oxidation and reduction processes when the scan rates increased from 0.1 to 100 mV s^{-1} can be observed in Fig. 5b. As shown in Fig. 5c, the peak separations between reduction peak and oxidation peak are

∼0.1 V in the scan rates range from 0.1 to 2 mV s^{-1}, demonstrating small polarization at high rates.[38]

Basing on the relationship between the scan rate (v) and the measured current (i):[42]

$$i = av^b \qquad [1]$$

where the power law relationship between measured current i and sweep rate v is observed. Here, a is an alterable parameter and b is the slope of the log(v)-log(i) plots obtained by CV curves. In especial, it is a total diffusion-controlled behavior when $b = 0.5$, and a capacitive process when $b = 1$. The log(v)-log(i) plots plotted from CV results of GF-CF are displayed in Fig. S2. In the scan rates range from 0.1 to 100 mV s^{-1}, we have calculated that b is about 0.6, indicating that the current mainly comes from the Na$^+$ inserting into GF-CF in the voltage window from 0.5 to 1.0 V, but capacitive process, which is in agreement with the study reported by Liming Wu et al. They proposed a reaction mechanism of anatase TiO$_2$ including the initial formation of an intermediately formed sodium titanate phase which disproportionates into another sodium titanate phase, metallic titanium, sodium superoxide, and later oxygen, but these processes are irreversible. Reversible sodium storage is due to Na$^+$ can reversibly insert/extract into/from the newly formed amorphous sodium titanate phase.[43]

According to the concepts presented above, current response can be distinguished into two parts, the one corresponding to surface capacitive effects, another corresponding to diffusion-controlled insertion process:[44]

$$i(V) = k_1 v + k_2 v^{1/2} \qquad [2]$$

For the purpose of analysis, Eq. 2 has been changed into

$$i(V)/v^{1/2} = k_1 v^{1/2} + k_2 \qquad [3]$$

In Eq. 2, $k_1 v$ represent the current contributions caused by the surface capacitive effects and $k_2 v^{1/2}$ represent diffusion-controlled intercalation process. Hence, if k_1 and k_2 were determined, the current
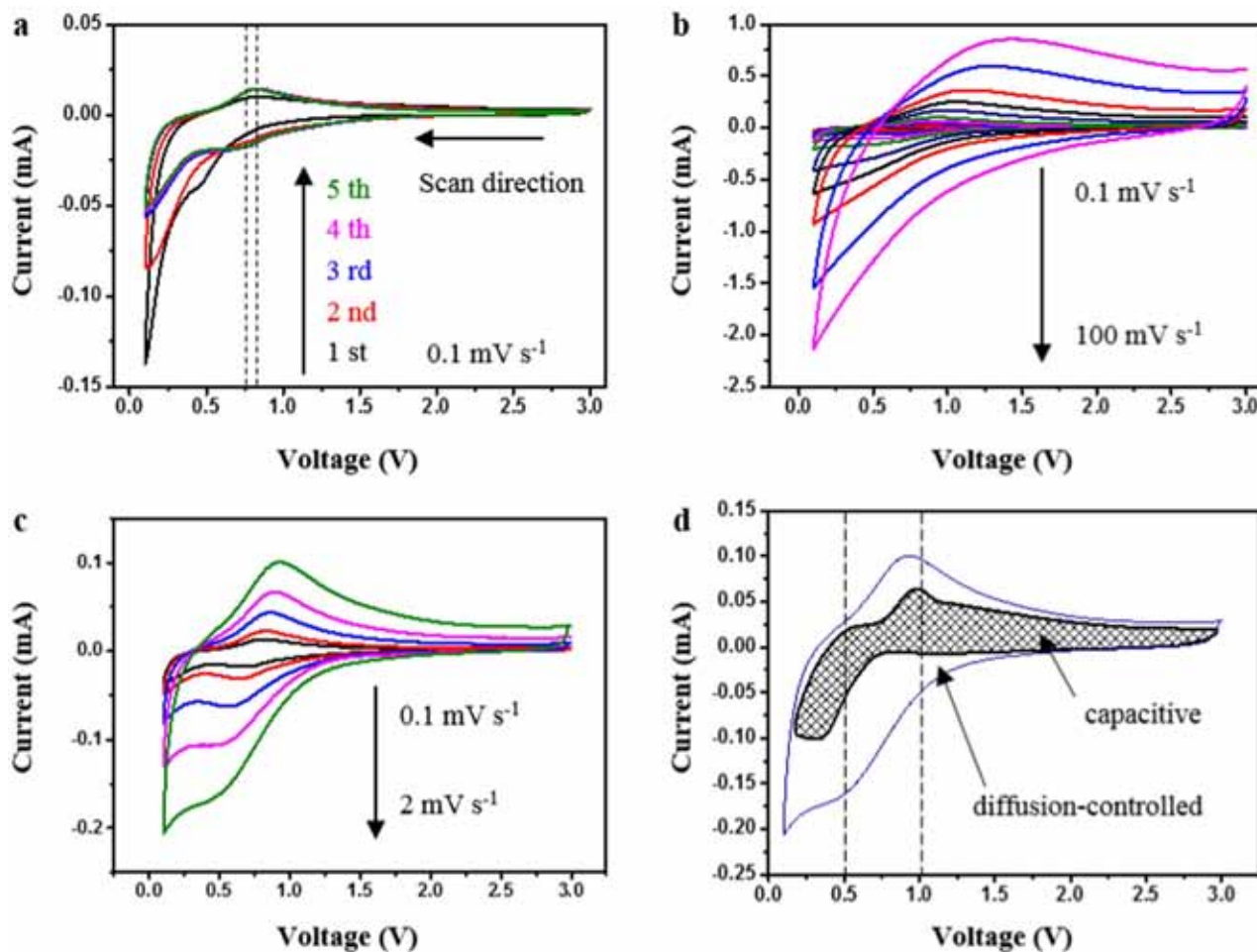
Figure 5. Kinetics analysis of the electrochemical behavior toward Na$^+$ for the GF-CF electrodes. (a) CV curves of GF-CF from 1st to 5th cycles at 0.1 mV s^{-1}; (b) CV curves of GF-CF at the scan rates range from 0.1 to 100 mV s^{-1}; (c) CV curves of GF-CF from 0.1 to 2 mV s^{-1}; (d) Na ions storage contributions from capacitive effects and diffusion-controlled process separated from CV curve at the scan rate of 2 mV s^{-1}.

originated from each of these contributions can be quantified at specific potentials. The current fitting results according to Eq. 3 are shown in Table S1, k_1 and k_2 were calculated from the linear fit in which corresponding to the slope and the y-axis intercept point. Using this way, we are able to tell apart the currents caused by sodium-ion insertion from measured total currents.

Based on the quantification in Fig. 5d, we are able to calculate the total stored charge and the respective contributions of both sodium insertion and capacitive processes. By comparing the shaded area with the total area, we have calculated the capacitive effects percentage of 45.1% in the total charge storage in the voltage window from 0.1 to 3.0 V at a scan rate of 2 mV s^{-1}. Especially, in the voltage window from 0.1 to 1.0 V the capacitive effects percentage is only 33.4%. On the basis of previous study,[45] the capacitive contributions from the smaller particles are significantly higher than those from the larger particles. So if the size of TiO$_2$ nanosheets that coaxially aligned on graphene foam could be diminished, the capacity of GF-CF will be improved significantly. In the voltage window from 0.5 to 1.0 V, current comes from the Na$^+$ diffusion higher than that comes from capacitive effects, the proportion of the diffusion-controlled current is 70.8%, which agree well with the b-value of ~0.6 (Fig. S2).

As shown in Fig. 6a, the specific discharge capacities of GF-CF are about 175, 142, 129, 96, 72, 40 and 154 mA h g^{-1} corresponding to the specific currents of 50, 100, 200, 500, 1000, 2000 and 50 mA g^{-1}, respectively. For comparison, rate performance of anatase TiO$_2$ and GF has been also tested under the same conditions. Obviously,

the specific capacity of GF-CF electrode at each rate is much higher than that of anatase TiO$_2$ and GF electrodes, indicating more effective transport for electron and Na$^+$ due to the coaxial frame structure of GF-CF. Meanwhile, the initial coulombic efficiency has been improved from 18% for anatase TiO$_2$ to 35% for GF-CF. To further investigate the cycle stability of GF-CF as anode materials for SIBs, GF-CF, anatase TiO$_2$ and GF has been tested at a specific current of 50 mA g^{-1}. After cycling for 100 cycles at 50 mA g^{-1}, GF-CF electrode delivers a discharge capacity of 136.0 mA h g^{-1} with coulombic efficiency of 96.5%, which is much higher than that of anatase TiO$_2$ electrode (96.1 mA h g^{-1}) and GF electrode (7.8 mA h g^{-1}) (Fig. 6b). And the capacity retention of GF-CF is 88.0% measured from the 10th cycle. Figs. 6c, 6d and 6e present the galvanostatic discharge–charge voltage profiles of GF-CF, anatase TiO$_2$ and GF in the potential window of 0.1–2 V at a specific current of 50 mA g^{-1}, respectively. As shown in Fig. 6c, upon the initial discharge, a slope profile occurs at ~0.2 V, involving disproportion reaction and formation of Ti^0 and O$_2$. An apparent voltage plateau at ~0.75 V appeared in the subsequent discharge due to Na$^+$ insertion and structural rearrangement, which agrees well with the CV results. The charge profile shows plateaus at ~0.84 V, which is due to the formation of Na$_x$(TiO$_2$).[43] The galvanostatic discharge-charge voltage profiles of TiO$_2$ (Fig. 6d) is similar to that of GF-CF, but specific capacities is lower because of the coaxial frame structure which ensures the fast electron transportation and the existence of large interface between graphene and TiO$_2$. According to previous studying,[38] the bonds between surface oxygen atoms of TiO$_2$ and carbon atoms of graphene are not entirely. Because some surface
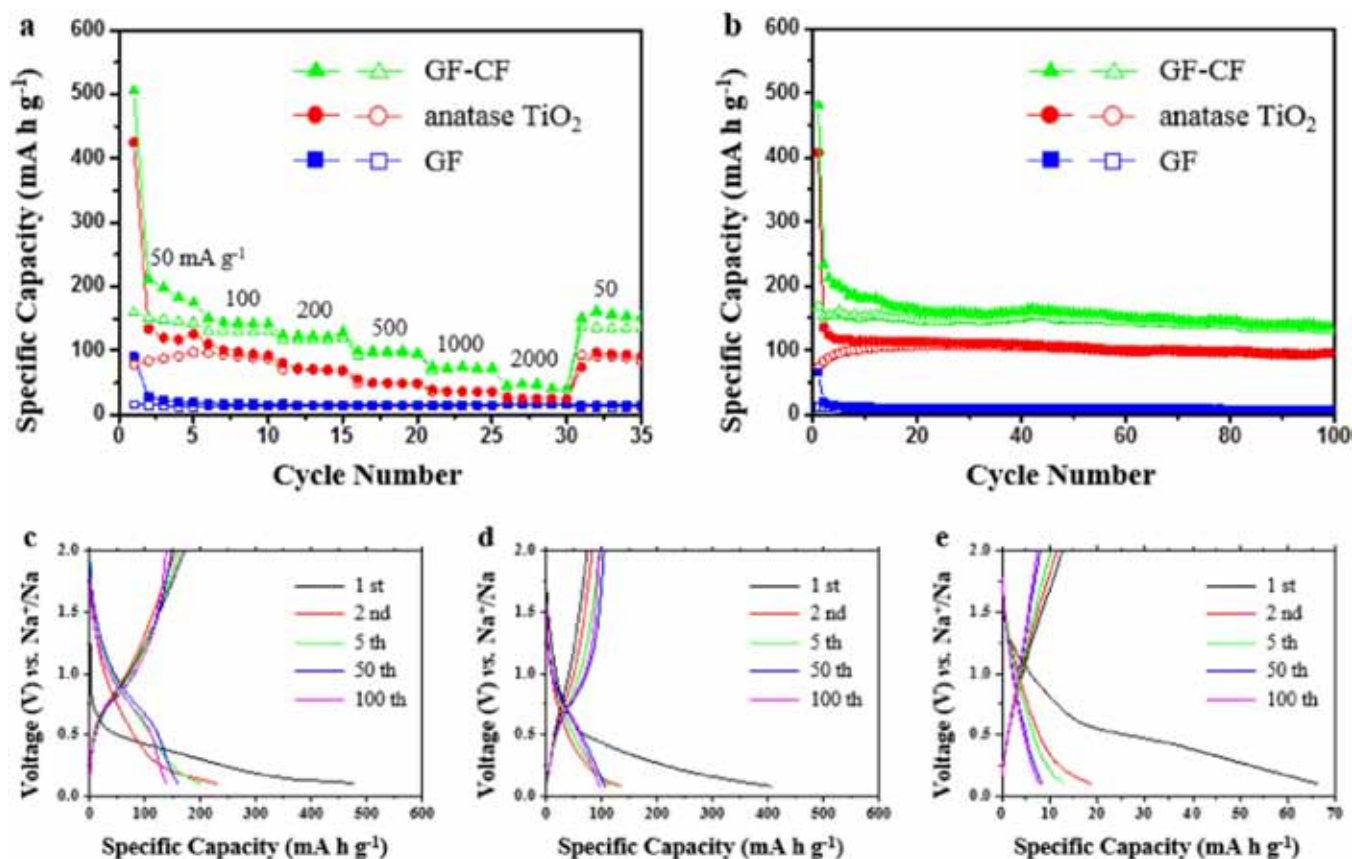
Figure 6. Electrochemical performance of GF-CF, anatase TiO_2 and GF electrodes. (a) Comparative rate performance of GF-CF, anatase TiO_2 and GF at various current rates; (b) cycle performance of GF-CF, anatase TiO_2 and GF at specific current of 50 mA g^{-1}; galvanostatic charge–discharge voltage profiles of GF-CF (c), anatase TiO_2 (d) and GF (e).

O atoms would be passivated by a neighboring surface O atom forming Ti-O-O-Ti bonds or surface -OH groups forming Ti-O-H bonds, rather than the formation of Ti-O-C bonds. As a result, the activation energy barrier will reduce, which is more feasible for sodium transport. So to a certain degree, we think the improvement in our work is due to the incomplete chemically bonds between graphene and TiO_2, which makes the ion transport channel more unimpeded and more active sites in the interface between graphene and TiO_2. Therefore, improved rate performance and capacity benefit by the coaxial frame structure.

Conclusions

GF-CF composite materials have been ingeniously designed as freestanding electrodes for SIBs. GF-CF electrodes were successfully fabricated via chemical vapor deposition and hydrothermal process. TiO_2 nanosheets are coaxially aligned on graphene foam framework, which offer 3D conducting networks. The coaxial frame structure ensures the fast electron transportation and large interface between graphene and TiO_2 to store more sodium ions. And the in situ growth that inhibits the aggregation of TiO_2 nanosheets. Therefore, SIBs with GF-CF showed a discharge capacity of 136.0 mA h g^{-1} (capacity retention is 88.0%) after 100 cycles with coulombic efficiency of 96.5%. According to cyclic voltammetry analysis, we find that capacitive effects contributed 45.1% in the total charge storage. If the size of TiO_2 nanosheets that coaxially aligned on graphene foam could be diminished, the capacity of GF-CF will be improved significantly. This coaxial frame integration strategy of nanosheets can be extendedly applied to the design of electrode materials for supercapacitors or photocatalytic applications.

References

1. B. Dunn, H. Kamath, and J. M. Tarascon, *Science*, **334**(6058), 928 (2011).
2. J. B. Goodenough, *Energy Environ. Sci.*, **7**(1), 14 (2014).
3. L. H. Chu, M. C. Li, X. D. Li, Y. Wang, Z. P. Wan, S. Y. Dou, D. D. Song, Y. F. Li, and B. Jiang, *RSC Adv.*, **5**(61), 49765 (2015).
4. L. H. Chu, M. C. Li, Y. Wang, X. D. Li, Z. P. Wan, S. Y. Dou, and Y. Chu, *J. Nanomater.*, **2016**(4), 1 (2016).
5. X. D. Li, G. X. Wu, J. W. Chen, M. C. Li, W. Li, T. Y. Wang, B. Jiang, Y. He, and L. Q. Mai, *Appl. Surf. Sci.*, **392**, 297 (2016).
6. X. D. Li, Y. Feng, M. C. Li, W. Li, H. Wei, and D. D. Song, *Adv. Funct. Mater.*, **25**(44), 6858 (2016).
7. W. Ren, Z. Zhu, Q. An, and L. Mai, *Small*, **13**(23), 1604181 (2017).
8. J. Y. Hwang, S. T. Myung, and Y. K. Sun, *Chem. Soc. Rev.*, **46**(12), 3529 (2017).
9. Y. Xu, M. Zhou, X. Wang, C. Wang, L. Liang, F. Grote, M. Wu, Y. Mi, and Y. Lei, *Angew. Chem. Int. Ed.*, **54**(30), 8768 (2015).
10. E. Irisarri, A. Ponrouch, and M. Palacin, *J. Electrochem. Soc.*, **162**(14), A2476 (2015).
11. F. Zhao, P. Xue, H. Ge, L. Li, and B. Wang, *J. Electrochem. Soc.*, **163**(5), A690 (2016).
12. G. H. Lee, M. R. Jo, K. Zhang, and Y. M. Kang, *J. Mater. Chem. A*, **5**(7), 3683 (2017).
13. J. S. Cho, J. S. Park, and Y. C. Kang, *Nano Res.*, **10**(3), 897 (2017).
14. G. Wang, X. Xiong, Z. Lin, C. Yang, Z. Lin, and M. Liu, *Electrochim. Acta*, **242**, 159 (2017).

15. Y. Xu, M. Zhou, L. Wen, C. Wang, H. Zhao, Y. Mi, L. Liang, Q. Fu, M. Wu, and Y. Lei, *Chem. Mater.*, **27**(12), 4274 (2015).
16. X. D. Li, W. Li, M. C. Li, P. Cui, D. H. Chen, T. Gengenbach, L. H. Chu, H. Y. Liu, and G. S. Song, *J. Mater. Chem. A*, **3**(6), 2762 (2014).
17. P. Cui, B. X. Xie, X. D. Li, M. C. Li, Y. Y. Li, Y. Wang, Z. H. Liu, X. Liu, J. Huang, and D. D. Song, *Crystengcomm*, **17**(41), 7930 (2015).
18. Z. Bi, M. P. Paranthaman, P. A. Menchhofer, R. R. Dehoff, C. A. Bridges, M. Chi, B. Guo, X. -G. Sun, and S. Dai, *J. Power Sources*, **222**, 461 (2013).
19. X. Su, Q. Wu, X. Zhan, J. Wu, S. Wei, and Z. Guo, *J. Mater. Sci.*, **47**(6), 2519 (2012).
20. M. A. Alim, T. Bak, A. Atanacio, J. D. Plessis, M. Zhou, J. Davis, and J. Nowotny, *J. Am. Ceram. Soc.*, **100**(9), 4088 (2017).
21. W. Li, F. Wang, Y. Liu, J. Wang, J. Yang, L. Zhang, A. A. Elzatahry, D. Al Dahyan, Y. Xia, and D. Zhao, *Nano Lett.*, **15**(3), 2186 (2015).
22. X. D. Li, G. X. Wu, G. X. Liu, W. Li, and M. C. Li, *Nano Energy*, **31**, 1 (2017).
23. X. Zhu, Q. Li, Y. Fang, X. Liu, L. Xiao, X. Ai, H. Yang, and Y. Cao, *Part. Part. Syst. Char.*, **33**(8), 545 (2016).
24. J. H. Kim, W. Choi, H. G. Jung, H. O. Si, K. Y. Chung, W. I. Cho, I. H. Oh, and I. W. Nah, *J. Alloy. Compd.*, **690**, 390 (2017).
25. J. W. Chen, M. Q. Cui, G. X. Wu, T. Y. Wang, J. M. Mbengue, Y. F. Li, and M. C. Li, *Carbon*, **116**, 133 (2017).
26. Y. F. Li, M. C. Li, T. Y. Wang, F. Bai, and Y. X. Yu, *Phys. Chem. Chem. Phys.*, **16**(11), 5213 (2014).
27. Y. F. Li, M. C. Li, T. S. Gu, F. Bai, Y. Yu, M. Trevor, and Y. X. Yu, *Appl. Surf. Sci.*, **284**(11), 207 (2013).
28. Y. F. Li, M. C. Li, T. S. Gu, F. Bai, Y. Yu, T. Mwenya, and Y. X. Yu, *Aip Advances*, **3**(5), 052130 (2013).
29. X. Q. Xie, T. Makaryan, M. Q. Zhao, K. L. Van Aken, Y. Gogotsi, and G. X. Wang, *Adv. Energy Mater.*, **6**, 1502161 (2015).
30. X. Yu, B. Lu, and Z. Xu, *Adv. Mater.*, **26**(7), 1044 (2014).
31. Z. P. Chen, W. C. Ren, L. B. Gao, B. L. Liu, S. F. Pei, and H. M. Cheng, *Nat. Mater.*, **10**(6), 424 (2011).
32. X. Yu, B. Lu, and Z. Xu, *Adv. Mater.*, **26**(7), 1044 (2014).
33. A. C. Ferrari, J. C. Meyer, V. Scardaci, C. Casiraghi, M. Lazzeri, F. Mauri, S. Piscanec, D. Jiang, K. S. Novoselov, and S. Roth, *Phys. Rev. Lett.*, **97**(18), 187401 (2006).
34. S. Huang, H. Yue, J. Zhou, J. Zhang, C. Zhang, X. Gao, and J. Chang, *Electroanal.*, **26**(1), 184 (2014).
35. Z. Chen, W. Ren, L. Gao, B. Liu, S. Pei, and H. M. Cheng, *Nat. Mater.*, **10**(6), 424 (2011).
36. W. Zhou, W. Li, J. -Q. Wang, Y. Qu, Y. Yang, Y. Xie, K. Zhang, L. Wang, H. Fu, and D. Zhao, *J. Am. Chem. Soc.*, **136**(26), 9280 (2014).
37. J. Shen, Y. Hu, M. Shi, X. Lu, C. Qin, C. Li, and M. Ye, *Chem. Mater.*, **21**(15), 3514 (2009).
38. C. Chen, Y. Wen, X. Hu, X. Ji, M. Yan, L. Mai, P. Hu, B. Shan, and Y. Huang, *Nat. Commun.*, **6**, 6929 (2015).
39. M. Chen, D. Chao, J. Liu, J. Yan, B. Zhang, Y. Huang, J. Lin, and Z. X. Shen, *Adv. Funct. Mater.*, **27**(12), 1606232 (2017).
40. L. Wu, J. Lang, R. Wang, R. Guo, and X. Yan, *ACS Appl. Mater. Interfaces*, **8**(50), 34342 (2016).
41. Y. Wu, X. Liu, Z. Yang, L. Gu, and Y. Yu, *Small*, **12**(26), 3522 (2016).
42. H. Lindström, S. Södergren, A. Solbrand, H. Rensmo, J. Hjelm, A. Hagfeldt, and S. E. Lindquist, *J. Phys. Chem. B*, **101**(39), 7717 (1997).
43. L. Wu, D. Bresser, D. Buchholz, G. A. Giffin, C. R. Castro, A. Ochel, and S. Passerini, *Adv. Energy Mater.*, **5**(2) (2015).
44. T. Liu, W. Pell, B. Conway, and S. Roberson, *J. Electrochem. Soc.*, **145**(6), 1882 (1998).
45. J. Wang, J. Polleux, J. Lim, and B. Dunn, *J. Phys. Chem. C*, **111**(40), 14925 (2007).